We are IntechOpen, the world's leading publisher of Open Access books Built by scientists, for scientists

4,800
Open access books available

122,000
International authors and editors

135M
Downloads

Our authors are among the

154
Countries delivered to

TOP 1%
most cited scientists

12.2%
Contributors from top 500 universities

WEB OF SCIENCE™

Selection of our books indexed in the Book Citation Index in Web of Science™ Core Collection (BKCI)

Interested in publishing with us?
Contact book.department@intechopen.com

Numbers displayed above are based on latest data collected.
For more information visit www.intechopen.com

8

Characterization of Room-Temperature Ferromagnetic $Zn_{1-x}Co_xO$ Nanowires

Yi-Ching Ou[1], Zhong-Yi Wu[2], Fu-Rong Chen[2],
Ji-Jung Kai[2] and Wen-Bin Jian[1]
[1]*National Chiao Tung University,*
[2]*National Tsing Hua University,*
Taiwan

1. Introduction

The manipulation and detection of an electron's charge and, simultaneously, its spin orientation in electronic devices have been developed to be a new emerging field of spintronics (or magnetoelectronics) (Prinz, 98; Wolf et al., 2001). At present, the most notable spintronic applications could be the hard disk read heads and the magnetic random access memory which are based on metal magnetic materials and are assorted into *metallic* spintronic devices. The establishment of metallic spintronics might be ascribed to a discovery of giant magnetoresistance (Baibich et al., 1988; Binasch et al., 1989) and, subsequently, understanding and exercise of a spin-valve scheme (Moodera et al., 1995), and tunnelling magnetoresistance (Dieny et al., 1991) in ferromagnetic multilayers. On the other hand, in order to integrate with the modern industrial technology, new semiconductor materials such as diluted magnetic semiconductors (DMSs) (Furdyna, 1988), also known as ferromagnetic semiconductors (Ohno, 1998), have been searched for a supply of a spin-polarized carrier source. Those devices building on a transport of spin current in semiconductors are categorized into *semiconductor* spintronics. Spin injection, maintenance of a spin coherence, spin detection, and a spin carrier source in semiconductors are all important issues for semiconductor spintronics.

The DMSs, based on host materials of II-VI and IV-VI semiconductors, have been studied for several decades. Although the indirect exchange mechanisms between *3d* transition metal dopants in these semiconductors have been inspected experimentally and discussed theoretically (Story et al., 1986; Sawicki et al., 1986; Furdyna, 1988) for a long time, the Curie temperature (T_C), below which a spontaneous magnetization and a spin-polarized current in the DMSs arise, was too low to be capable of employment. Until recent advance in III-V DMSs of (In,Mn)As and (Ga,Mn)As (Ohno et al., 1996), T_C's of some new DMSs such as (Ga,Mn)As have been raised up to ~110 K. These new III-V DMS materials were exploited to demonstrate tunneling magnetoresistance in (Ga,Mn)As ultrathin heterostructures (Hayashi et al., 1999), electrical spin injection in a ferromagnetic semiconductor heterostructure (Ohno et al., 1999), electric-field control of ferromagnetism (Ohno et al., 2000}, electrical manipulation of magnetization reversal (Chiba et al., 2003), and current-induced domain-wall switching (Yamanouchi et al., 2004). On the other hand, the other approach of spin-current injection into semiconductors from ferromagnetic metals has recently been achieved, so as to realize semiconductor spintronics at room temperature.

Source: Nanowires, Book edited by: Paola Prete,
ISBN 978-953-7619-79-4, pp. 414, March 2010, INTECH, Croatia, downloaded from SCIYO.COM

By using Zener model description, Dietl et al. (Dietl et al., 2000) have theoretically sustained the fact of a 110-K high T_C for *p*-type (Ga,Mn)As with a manganese concentration of just 5%. In addition, they argued the presence of a T_C above room temperature in Mn doped ZnO or GaN with hole carriers of 3.5×10^{20} cm^{-3}. These theoretical arguments drew much attention on search for room-temperature ferromagnetism (RTFM) in new DMS materials. For example, Matsumoto et al. (Matsumoto et al., 2001) discovered RTFM in Co doped TiO_2 with a magnetic moment of 0.32 Bohr magneton (μ_B) per Co atom and Toyosaki et al. (Toyosaki et al., 2004) observed anomalous Hall effect in this particular material. Else, Ueda et al. descried ferromagnetism and a T_C above 280 K in pulse laser deposited $Zn_{1-x}Co_xO$ films (Ueda et al., 2001). Cho et al. found ferromagnetic and antiferromagnetic ordering in $(Zn_{1-x}Mn_x)GeP_2$ at temperatures up to 312 K and below 47 K (Cho et al., 2002), respectively. Among all new as-proposed DMS materials, Co-doped metal oxides, such as $Ti_{1-x}Co_xO_2$ and $Zn_{1-x}Co_xO$, seem to be an appropriate candidate for a spin-polarized carrier source at room temperature (Janisch et al., 2005).

ZnO is recently a hot material and it is proposed to be valuable in many application fields such as blue/ultraviolet optoelectronics (Klingshirn, 2007; Pearton et al., 2004). It is a direct and wide band gap semiconductor and can be easily over-doped to form conductive and transparent films. ZnO is natively *n*-type doped to show relatively lower resistivity due to difficulties in control of point defects during the growth process. In addition, it shows ultraviolet (near band edge) and green (or blue) defect emission at ~3.2 and ~2.5 eV, respectively, in photoluminescence (PL) spectra. It is proposed that oxygen vacancies (Lanny & Zunger, 2005), zinc interstitials (Look et al., 1999), Zn_I-N_O complexes (Look et al., 2005), metastable conductive states (Lany & Zunger, 2007), or hydrogens (Van de Walle, 2000) can lead to the native *n*-type doping, the coloration, and the green emission. The point defects not only result in an increase of conductivity but also modulate magnetic ordering after ZnO is doped with paramagnetic *3d* transition metal dopants.

2. Important

There are so many experimental and theoretical reports on claiming that Co-doped ZnO is an intrinsically DMS (Schwartz & Gamelin, 2004; Coey et al., 2005; Neal et al., 2006; Zhang et al., 2009). Very recently, different magnetic mechanisms are uncovered in insulating and magnetic regimes (Behan et al., 2008). In particular, magnetic resistance has been observed in a magnetic tunnel junction fabricated by using Co-doped ZnO as one ferromagnetic electrode (Xu et al., 2008). There are, however, other contradictory reports exposing antiferromagnetism (Risbud et al., 2003), secondary phases in crystalline structure, clustering of Co metals or ions (Sati et al., 2007), or absence of ferromagnetism in this material. On the other hand, even for similar conclusions of ferromagnetism, the Curie temperature either above or below the room temperature is another issue. As we have emphasized, it is difficult to control point defects in ZnO during growth. Moreover, electrical resistivity and PL emission of a pure ZnO, and a magnetic ordering of a Co-doped ZnO can all be altered by thermal annealing after growth. Here we propose the employment of nanowires (NWs) for an exploration into magnetism because, after converted to a nanophase, the nanomaterials have a large surface to volume ratio, feasible for thermal treatments, and they are handy for a structural characterization by using transmission electron microscopy.

In our previous reports, we have observed the structure and annealing effect on ferromagnetic ordering (Jian et al., 2006; Wu et al., 2006), and have explored the size

dependent behavior (Jian et al., 2007) in $Zn_{1-x}Co_xO$ NWs. In addition, we have discovered RTFM in high-vacuum annealed $Zn_{1-x}Co_xO$ NWs (Chen et al., 2008) and the effect of cross-sectional shape modulation (Wu et al., 2008). In this chapter, we present complete characterizations, including structure, optical, and magnetic property measurements on pure ZnO NWs, as-implanted $Zn_{1-x}Co_xO$ NWs, annealed $Zn_{1-x}Co_xO$ NWs, and a comparative sample of ZnO NWs sheathed in amorphous carbon with Co clusters, so as to explore the mechanism of RTFM in the DMS of $Zn_{1-x}Co_xO$ NWs.

3. Experiment

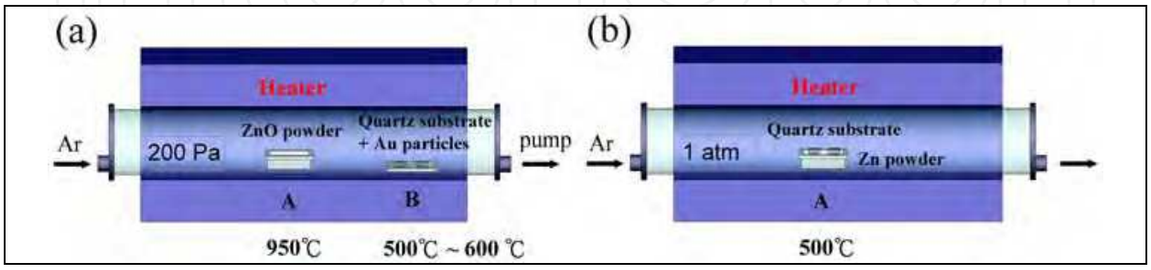

Fig. 1. Schematic illustration of the growth of pure ZnO NWs with (a) circular and (b) hexagonal cross sections.

Cylindrical and hexagonal ZnO NWs were grown by using a vapor-phase transport process. The growth of cylindrical ZnO NWs is schematically illustrated in Fig. 1(a). A quartz tube treated as a growth chamber was inserted in a furnace. ZnO powders were placed in a crucible in the growth chamber and heated to 950°C. The chamber was maintained at 200 Pa with a constant flow of argon and a pumping system. For a purpose of controlling NW diameter, gold nanoparticles as catalysts with specified average diameters of 5, 10, 20, 40, 70, and 100 nm were dispersed on quartz substrates. The substrates were positioned at the downstream end of the growth chamber and were maintained at 500-600°C. Cylindrical ZnO NWs with a controllable diameter were formed on substrates after a growth period of 8 h.

The growth of hexagonal ZnO NWs, as schematically illustrated in Fig. 1(b), is different from that of cylindrical NWs. Diameters of hexagonal NWs cannot be well regulated through the use of catalysts. During the synthesis process, Zn powders were placed in an alumina boat in the quartz tube chamber and heated to 500°C. The substrates were put on top of the alumina boat and the chamber was maintained at 1 atm with a constant flow of argon. Like the growth of cylindrical NWs, a 8-h synthesis period was retained for growth of hexagonal ZnO NWs. The crystalline structure and morphology of both cylindrical and hexagonal ZnO NWs were analyzed by using field-emission scanning electron microscope (SEM, JEOL JSM 7000F) and transmission electron microscope (TEM, JEOL JEM-2010F).

The as-grown ZnO NWs were implanted by Co ions with doses of (1-6) × 10^{16} cm^{-2}. By using a tandem accelerator (NEC 9SDH-2), the implantation was performed at room temperature. An accelerating energy of 72 keV was used for NWs with average diameters larger than ~70 nm. Thinner NWs were implanted by Co ions with an acceleration energy of 40 keV. A beam current of either 150 or 600 nA/cm^2 was used to make $Zn_{1-x}Co_xO$ NWs. The high bean current of 600 nA/cm^2 could somewhat turn out to be thermal treatment due to the high energy ion bombardment in a high vacuum. The fabrication process is schematically drawn in Fig. 2(a) and its corresponding side-view SEM image of the $Zn_{1-x}Co_xO$ and ZnO NWs is

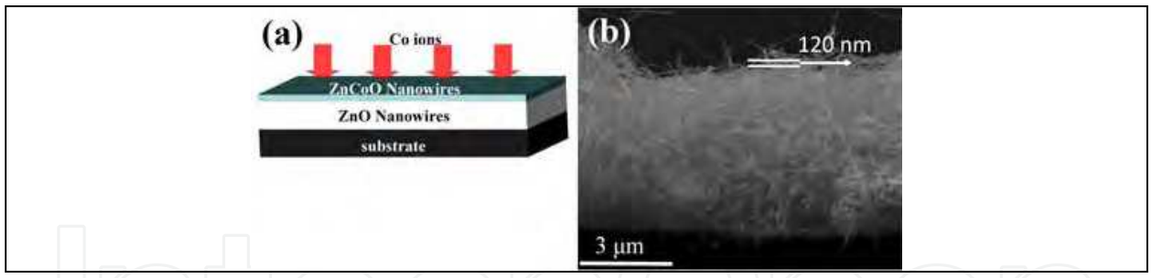

Fig. 2. (a) Schematic illustration of Co ion implantation. (b) Side-view SEM image of cylindrical ZnO NWs on a quartz substrate.

displayed in Fig. 2(b). As indicated in the figure, only a ~120-nm thin layer of $Zn_{1-x}Co_xO$ NWs could be formed on ~3-μm thick layer of pure ZnO NWs (Wu et al., 2006). The chemical composition as well as Co element distribution in $Zn_{1-x}Co_xO$ NWs were inspected through energy dispersive x-ray (EDX) and electron energy loss spectroscopy (EELS) mapping. In order to study the origins of ferromagnetism in $Zn_{1-x}Co_xO$ NWs, some specimens were post-annealed in argon, in a high vacuum of 5×10^{-5} torr, or in oxygen at 600°C (or 450°C) for several hours. In particular, multiple steps of thermal annealing in a high vacuum were carried out to produce a gradual transition of magnetic states of this DMS material. PL spectra of some specimens were measured at room temperature by using a 325-nm He-Cd laser as UV fluorescent light excitation.

In addition to DMS $Zn_{1-x}Co_xO$ NWs, ZnO NWs sheathed in amorphous carbon with Co clusters were produced for comparison. These purposely fabricated samples were treated with the same thermal annealing process as that for DMS NWs. Co metal clusters in carbon-coated ZnO NWs were intriguingly formed after a high-vacuum annealing. The morphology, crystalline structure and chemical composition of these comparative samples were analyzed in a similar way.

Magnetic properties of DMS $Zn_{1-x}Co_xO$ NWs and comparative samples (Co clusters on ZnO NWs) were measured by employing a SQUID magnetometer (Quantum Design MPMS-XL7) with the reciprocating sample option mode. Field cool (FC) and zero-field cool (ZFC) processes were conducted to obtain temperature dependent magnetization during the rising temperature sequence under an external magnetic field of 500 Oe. That is, the samples were subjected to oscillating with decreasing fields and were cooled from 300 K down to 2 K in a zero field. The samples were then warmed up to obtain ZFC magnetization as a function of temperatures in 500 Oe. They were cooled down in the same field and warmed up again to record the FC magnetization. Before NW growth, the magnetic susceptibility of a quartz substrate was estimated to be $\sim -1.1 \times 10^{-6}$ emu/cm^3 so that diamagnetic contribution of the substrate can be subtracted from the total magnetization. Magnetic data were presented in unit of μ_B per Co where the amount of Co ions was evaluated by multiplying the ion dose per cm^2 with the substrate area.

4. Growth, morphology, crystalline structure, and photoluminescence

In this section, the growth behavior of pure ZnO NWs is discussed. The morphology, crystalline structure, and optical properties of as-grown ZnO, as-implanted $Zn_{1-x}Co_xO$, high-vacuum annealed $Zn_{1-x}Co_xO$, and ZnO NWs sheathed in amorphous carbon with Co clusters are inspected by using electron microscopy and PL spectra analyses.

4.1 Growth behavior

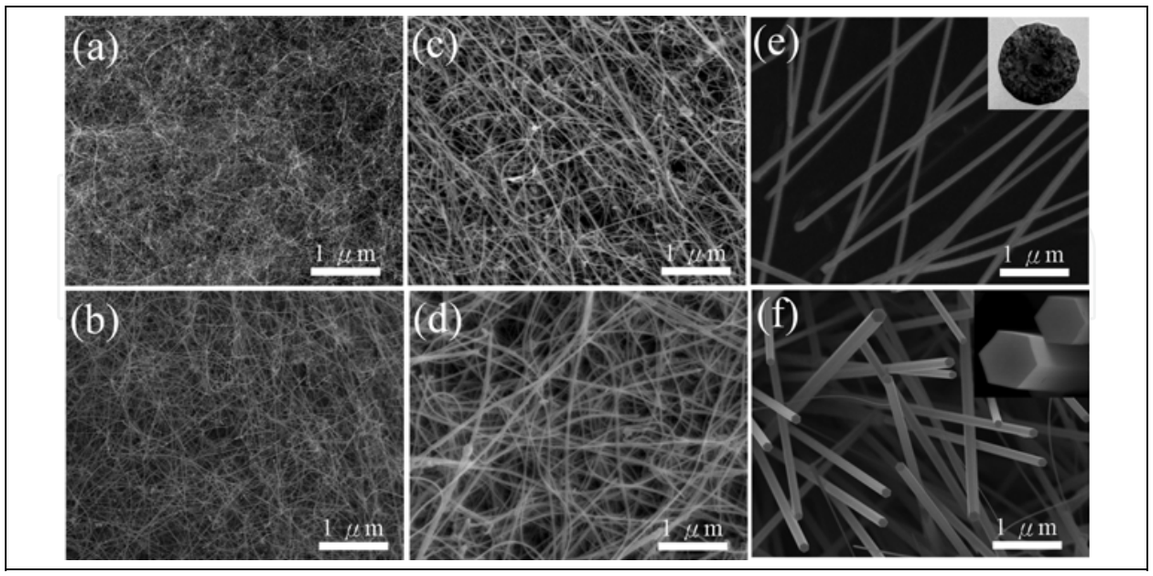

Fig. 3. SEM images of as-grown cylindrical ZnO NWs with average diameters of (a) 7 nm, (b) 12 nm, (c) 19 nm, (d) 38 nm, and (e) 113 nm. (f) SEM image of as-grown hexagonal ZnO NWs with an average diameter of 134 nm. The insets of Figs. 3(e) and (f) display cross-sections of cylindrical and hexagonal ZnO NWs, respectively.

Figures 3(a)-(e) display SEM images of cylindrical ZnO NWs with increasing average diameters and Fig. 3(f) displays a SEM image of hexagonal ZnO NWs. The cylindrical NWs with average diameters of 7, 12, 19, 38, and 113 nm were grown by using gold-nanoparticle catalysts with average sizes of 5, 10, 20, 40, and 100 nm, respectively. The NWs displaying in the same magnification SEM images demonstrate obviously distinct dimensions, implying a very well control of the NW diameter through the size of gold nanoparticles. In addition, the surface morphology of cylindrical NWs appearing in the inset of Fig. 3(e) indicates that the cross-section of ZnO NWs certainly conforms to the circular shape of gold nanoparticles. A different synthesis method resulting in an either circular or hexagonal cross-section could be discerned in the insets of Figs. 3(e) and (f). Besides, we have noticed a more and more curved feature for cylindrical ZnO NWs as compared with hexagonal ones, and for thinner NWs as compared with thicker ones. The same growth period of 8 h is kept and a considerably high density of small diameter NWs could be observed unambiguously in SEM images.

Figure 4 displays statistical information of diameters of our as-grown ZnO NWs. In Fig. 4(a), we demonstrate a representable diameter distribution of cylindrical ZnO NWs with a 12-nm average diameter. The standard deviation of the 12-nm diameter NWs is evaluated to be 2.7 nm (23%). This somewhat large deviation in NW diameter may come from a broad size distribution of our catalysts, gold nanoparticles, which is not investigated in this experiment yet. In contrast, Fig. 4(b) reveals a flat diameter distribution, indicating a large diameter deviation of hexagonal ZnO NWs, due to a disparate growth behaviour. The average diameter and standard deviation of hexagonal NWs are estimated to be about 134 nm and 74 nm (55%), respectively. Figure 4(c) reveals the average diameters and standard deviations of cylindrical ZnO NWs as a function of sizes of gold nanoparticles. A highly

linear correlation between the nanoparticle and the NW diameters firmly corroborate again a well control of the NW diameter.

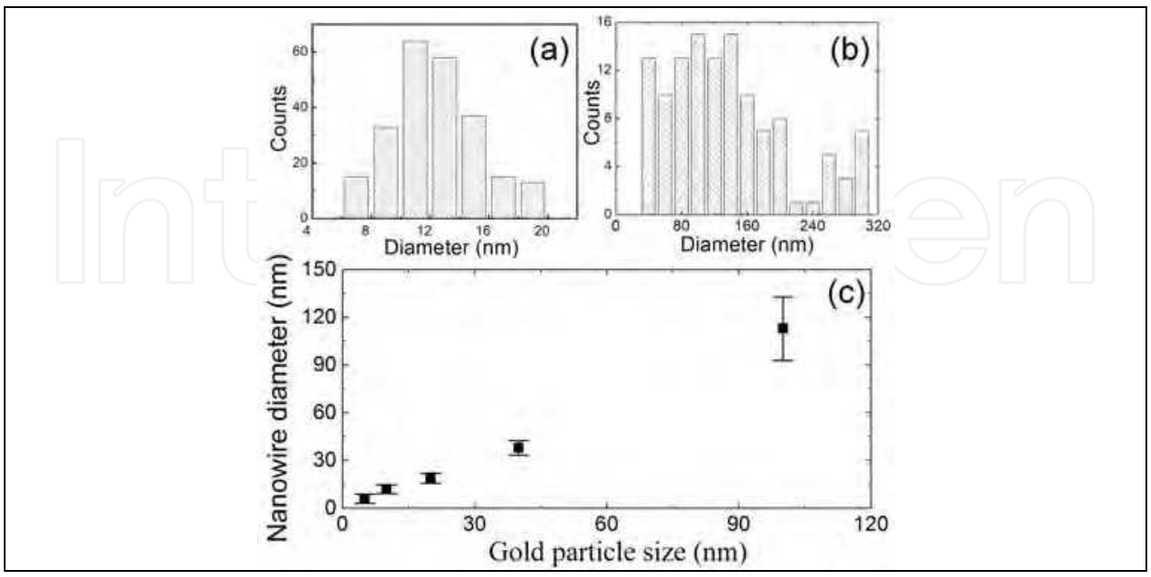

Fig. 4. (a) A typical statistical distribution of NW diameters for cylindrical ZnO NWs having an average diameter of 12 nm. (b) A statistical distribution of NW diameters for hexagonal ZnO NWs. (c) The average diameters with standard deviations of cylindrical NWs as a function of the diameter of the gold nanoparticles (catalysts).

4.2 Morphology and crystalline structure

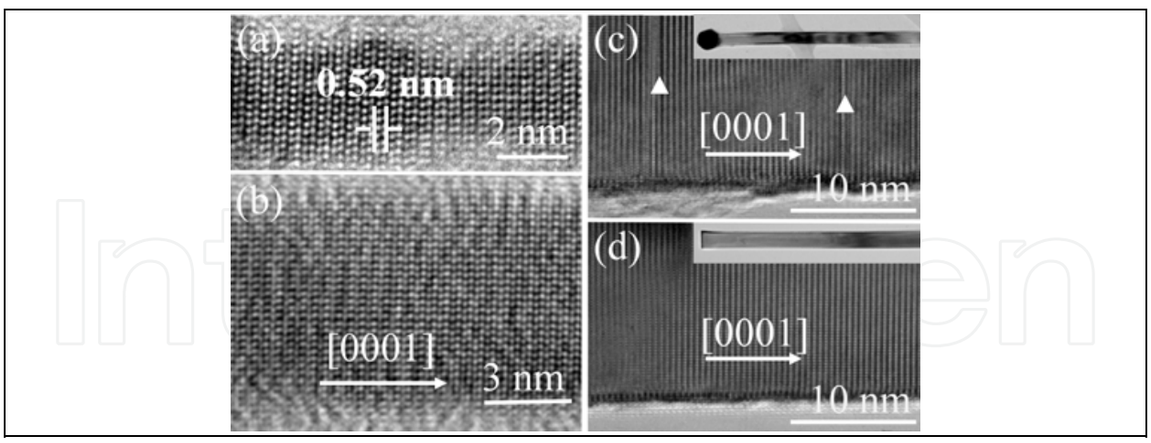

Fig. 5. High-resolution TEM images of as-grown cylindrical ZnO NWs with average diameters of (a) 7 nm, (b) 12 nm, and (c) 38 nm. (d) High-resolution TEM image of hexagonal ZnO NWs with an average diameter of 134 nm. The upper right insets in Figs. 5(c) and (d) show TEM images of as-grown ZnO NWs at low magnification. The upper triangles marked in Fig. 5(c) point to the planar defects of stacking faults.

Four representative high-resolution TEM images of as-grown cylindrical ZnO NWs with average diameters of 7, 12, and 38 nm are presented in Figs. 5(a), (b), and (c), respectively. A

double layer spacing of 0.52 nm agrees well with the *c* lattice constant of a ZnO wurtzite crystal structure that also denotes the [0001] growth direction. A single crystalline structure in different average diameters of either cylindrical or hexagonal ZnO NWs has been inspected and verified. The insets in Figs. 5(c) and (d) demonstrate TEM images of cylindrical and hexagonal ZnO NWs, respectively, at low magnification. A gold nanoparticle sitting on one end of the cylindrical ZnO NW is observed in Fig. 5(c) as well. Further, as exhibited in Fig. 5(a), a nanoscale bumper edge surface is more evidently observed on thiner and cylindrical NWs than on thicker and hexagonal NWs. Moreover, many stacking faults, designating by upper triangles in Fig. 5(c), are identified in cylindrical NWs.

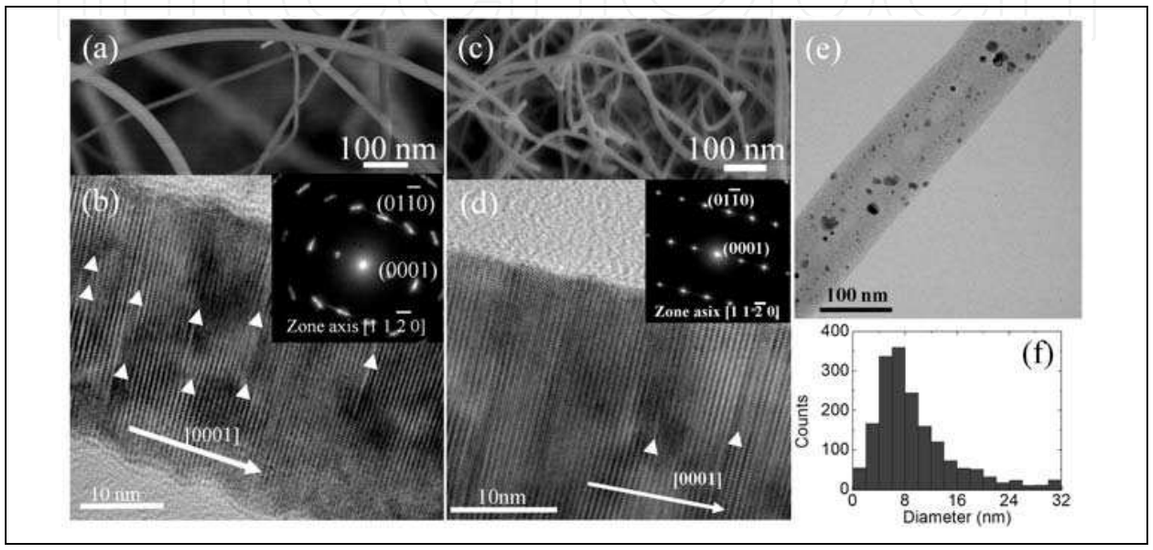

Fig. 6. SEM images of (a) as-implanted and (c) high-vacuum annealed $Zn_{1-x}Co_xO$ NWs with an average diameter of 38 nm and a Co ion does of 6×10^{16} cm^{-2}. High resolution TEM images of (c) as-implanted and (d) high-vacuum annealed $Zn_{1-x}Co_xO$ NWs. The insets in Figs. 6(b) and (d) display corresponding electron diffraction patterns. (e) TEM image of a ZnO NW sheathed in carbon amorphous with Co clusters after high-vacuum annealing. (f) Statistical distribution of Co-cluster diameters estimated from TEM images. The average diameter and standard deviation are 9.4 and 6.0 nm, respectively.

As-grown and pure ZnO NWs were doped by high energy Co ions to form $Zn_{1-x}Co_xO$ NWs. SEM and TEM images of $Zn_{1-x}Co_xO$ NWs with an average diameter of 38 nm and a Co ion dose of 6×10^{16} cm^{-2} are demonstrated in Figs. 6(a) and (b). In Fig. 6(a), the bending feature of as-implanted $Zn_{1-x}Co_xO$ NWs is appreciable. In addition, the as-implanted $Zn_{1-x}Co_xO$ NWs consist of lots of stacking faults, as designated by triangles in Fig. 6(b), and they exhibit a streaking of an electron diffraction pattern (see the inset). Although the bending feature can be detected in as-grown ZnO NWs, more and more stacking faults and an obvious streaking in an electron diffraction pattern are discovered in as-implanted $Zn_{1-x}Co_xO$ NWs. It is proposed that these structure defects could mainly come from a high-energy Co ion bombardment during the ion implantation process. After a high-vacuum annealing, SEM and TEM images of the same sample are shown in Figs. 6(c) and (d). We can see that the stacking faults (indicated as triangles in Fig. 6(d)) and streaking are removed after a thermal treatment. We notice that an annealing at 600°C could help to recover structure disorders and defects. We also found that annealing at a higher temperature may cause a meltdown of

ZnO NWs. A lower annealing temperature of 450°C was thereafter applied to subsequent experiments and no noticeable changes in morphology were observed after the thermal treatment.

In order to study the magnetic mechanism in $Zn_{1-x}Co_xO$ NWs, we have made a comparative sample, ZnO NWs sheathed in amorphous carbon by Co ion implantation. There are neither perceptible clusters nor nanocrystals before any thermal treatments (not shown in figures). After a high-vacuum annealing, Co clusters, having a broad size distribution, could be discovered in TEM images. Figures 6(e) and (f) show a typical TEM image of the Co clusters and a statistical distribution of diameters. The 40-nm diameter ZnO NW is embedded in a shell of carbon amorphous with a diameter of ~100 nm. The average diameter and standard deviation of the Co clusters are about 9.4 and 6.0 nm, respectively. This sample was fabricated by Co ion implantation with a dose of 4×10^{16} cm^{-2} and post-annealed in a high vacuum at 600°C. In contrast to the high-vacuum annealed $Zn_{1-x}Co_xO$ NWs, in which Co cluster have never been detected in TEM images (Fig. 6(d)), the sample of ZnO sheathed in amorphous carbon with Co-ion implantation exhibits obviously many Co clusters after a high-vacuum annealing. The result suggests that Co ions may have a longer diffusion length in amorphous carbon than that in ZnO.

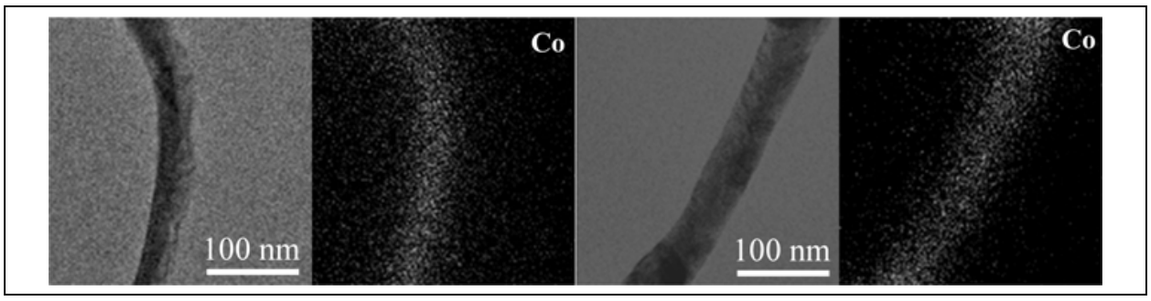

Fig. 7. TEM images of (a) as-implanted and (c) high-vacuum annealed $Zn_{1-x}Co_xO$ NWs with a dose of 6×10^{16} cm^{-2} and an average diameter of 38 nm. EDX mapping images of the Co element in (b) as-implanted and (d) high-vacuum annealed $Zn_{1-x}Co_xO$ NWs.

To identify Co ion distribution in $Zn_{1-x}Co_xO$ NWs, a EDX mapping of the Co element is employed. Figures 7(a) and (b) present TEM and EDX mapping images of as-implanted $Zn_{1-x}Co_xO$ NWs. For comparison, TEM and EDX mapping images of high-vacuum annealed $Zn_{1-x}Co_xO$ NWs are given in Figs. 7(c) and (d). Under the spatial resolution of the EDX chemical mapping, no perceptible aggregation of Co ions has ever been detected in all high-vacuum annealed $Zn_{1-x}Co_xO$ NWs. The results are in line with the TEM measurements shown in Fig. 6. We concluded, therefore, that a low temperature thermal treatment (below 600°C) can induce a recovery of a structure disorder but not a diffusion and aggregation of Co ions. Moreover, a high resolution technique, the compositional mapping of electron energy loss spectroscopy, a confirmation of a non-aggregated distribution of Co element in both as-implanted and high-vacuum annealed $Zn_{1-x}Co_xO$ NWs (Chen et al., 2008). Chemical compositions of $Zn_{1-x}Co_xO$ NWs were determined by using EDX spectra (Jian et al., 2007). Average Co-concentrations of $Zn_{1-x}Co_xO$ NWs were decided to be 2, 4, 6, 8, 10, and 11% for ZnO NWs with Co ion doses of 1, 2, 3, 4, 5, and 6×10^{16} cm^{-2}, respectively. The variation of NW diameters does not affect the average Co-concentration but causes a large standard deviation of Co-concentration in thinner $Zn_{1-x}Co_xO$ NWs.

4.3 Photoluminescence spectra

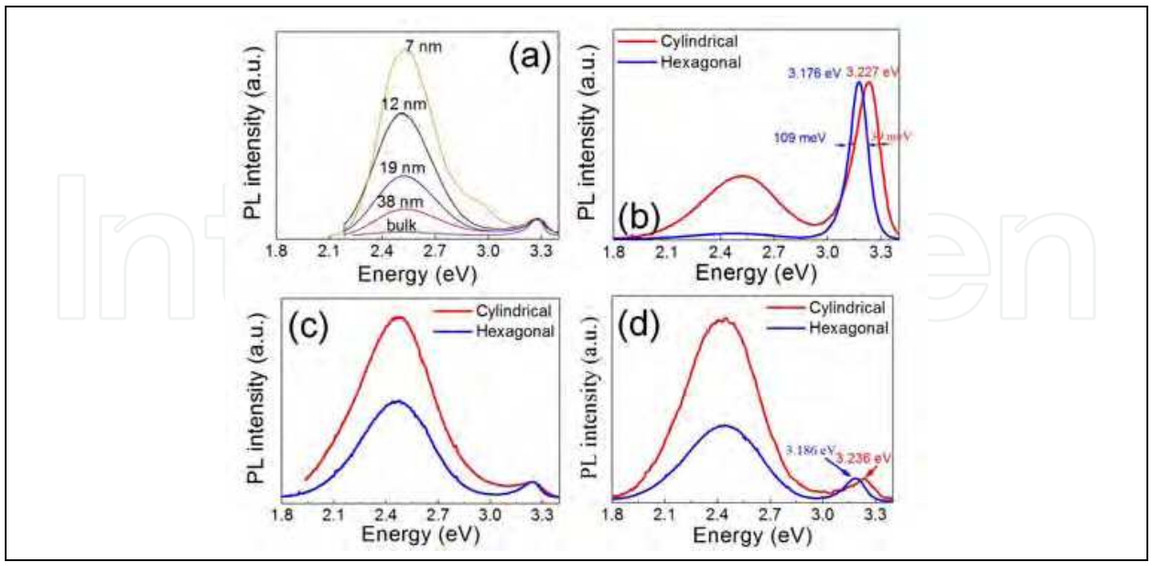

Fig. 8. (a) Room temperature PL spectra of as-grown (pure) ZnO bulk and NWs with average diameters as indicated on graph. Room temperature PL spectra of (b) as-grown, (c) as-implanted, and (d) high-vacuum annealed $Zn_{0.89}Co_{0.11}O$ NWs with average diameters of 113 and 134 nm for cylindrical and hexagonal cross sections.

The PL spectra of as-grown ZnO, as-implanted $Zn_{1-x}Co_xO$, and high-vacuum annealed $Zn_{1-x}Co_xO$ NWs are presented in Fig. 8. PL attributes show a green defect emission at ~2.5 eV and a near band edge emission at ~3.2 eV. The peak of the near band edge emission is normalized to be of the same height for a easy comparison of the defect emission. Figure 8(a) exhibits PL spectra of NWs with several average diameters. It shows that the intensity of the green emission (near band emission) is relatively higher (lower) for thinner ZnO NWs. As mentioned above, thinner NWs were examined to have a high density of structure defects (stacking faults), a bumper surface, and a curved feature. The green defect emission might be in connection with structure defects such as point defects of oxygen vacancies and zinc interstitials since an increase of point defects may cause a generation of more planar defects (stacking faults).

Figures 8(b), (c), and (d) present PL spectra of as-grown, as-implanted, and high-vacuum annealed $Zn_{0.89}Co_{0.11}O$ NWs with average diameters of 113 and 134 nm for cylindrical and hexagonal cross sections. The as-implanted $Zn_{0.89}Co_{0.11}O$ NWs exhibit a much higher intensity of a green emission (Fig. 8(c)) while the high-vacuum annealed NWs show a lower green emission peak (Fig. 8(d)). This result marks a correlation between the structure defects and the green emission as well. In addition to an intensity change of the defect emission, Fig. 8(b) points to a shift of the near band edge emission from 3.178 eV (cylindrical) to 3.227 eV (hexagonal) for as-grown ZnO NWs. Both cylindrical and hexagonal, as-implanted NWs reveal a blue shift in the near band edge emission peak (see Fig. 8(c)). After annealing in a high vacuum, the blue shift disappears and the band emission peaks move back to 3.186 and 3.236 eV for cylindrical and hexagonal $Zn_{0.89}Co_{0.11}O$ NWs, respectively. Though structure defects, strains, and surface effects (surface roughness) could all be the rationales, we believe that the anomalous blue shift could predominantly come from the surface effects.

5. Magnetic properties

The morphology and structure analyses indicate that Co-ions are randomly disributed without aggregation in as-implanted and high-vacuum annealed $Zn_{1-x}Co_xO$ NWs. Meanwhile, the high-vacuum annealing will induce an aggregation of Co ions in amorphous carbon coated on ZnO NWs and result in Co clusters. In this section, a SQUID magnetometer is employed to study temperature and field dependent behaviours of as-implanted $Zn_{1-x}Co_xO$, high-vacuum annealed $Zn_{1-x}Co_xO$, and ZnO NWs sheathed in amorphous carbon with Co clusters.

5.1 Temperature dependent magnetization

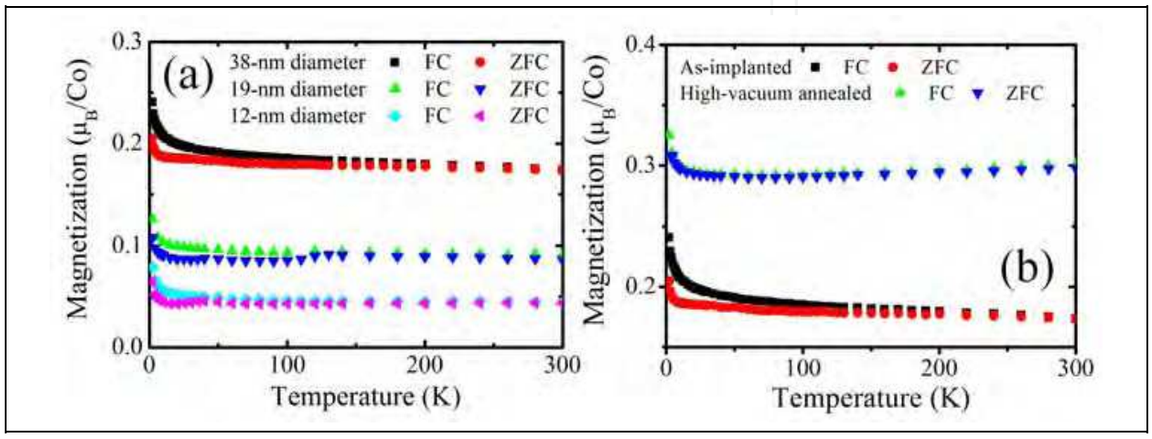

Fig. 9. (a) FC and ZFC behaviors of temperature dependent magnetization of as-implanted $Zn_{0.92}Co_{0.08}O$ NWs with average diameters of 12, 19, and 38 nm. (b) FC and ZFC magnetizations of as-implanted and high-vacuum annealed $Zn_{0.92}Co_{0.08}O$ NWs with an average diameter of 38 nm. The annealing time is 12 h.

In a magnetic field of 500 Oe, temperature dependent magnetizations of various average diameters of $Zn_{0.92}Co_{0.08}O$ NWs are shown in Fig. 9(a). The magnetization per Co ion of as-implanted $Zn_{0.92}Co_{0.08}O$ NWs depends strongly on the NW diameter. Thicker NWs exhibit higher magnetization. In addition, magnetizations under field cooled (FC) and zero-field cooled (ZFC) procedures show a division into two separate curves with decreasing temperature. In a similar way, the transition temperature, at which the FC and ZFC magnetization curves bifurcate, is higher for the thicker NWs. The difference in FC and ZFC magnetization suggests an existence of small magnetic domains in $Zn_{0.92}Co_{0.08}O$ NWs. In addition, the high transition temperature implies larger magnetic domains existing in thicker NWs.

In a previous report (Chen et al., 2008), we argued that either oxygen vacancies or zinc interstitials could result in a ferromagnetic coupling between the Co ions. It is conjectured that the as-implanted $Zn_{0.92}Co_{0.08}O$ NWs consist of the same concentration of oxygen vacancies (zinc interstitials) so the size of magnetic domains of non-aggregated Co ions may be larger in thicker NWs. On the other hand, the size dependent magnetization and hysteresis loop could be owing to the generation of planar defects, stacking faults and streaking, during the ion bombardment process (Jian et al., 2006). Moreover, planar defects could hinder an oxygen-vacancy mediated ferromagnetic ordering so as to abate magnetization and coercivity of thinner, as-implanted $Zn_{1-x}Co_xO$ NWs.

Figure 9(a) displays a non-vanishing and non-decreasing magnetization up to a room temperature, signifying a ferromagnetic ordering as well as RTFM. After annealing in a high vacuum, the temperature behavior of $Zn_{0.92}Co_{0.08}O$ NWs with an average diameter of 38 nm is displayed in Fig. 9(b), including reproduced data of as-implanted NWs for comparison. The temperature behavior demonstrates a much higher magnetization (a strong ferromagnetic state) and a coincidence and overlapping of FC and ZFC magnetization. This result indicates a growth and development of large magnetic domains, formed by non-aggregated Co ions in high-vacuum annealed $Zn_{0.92}Co_{0.08}O$ NWs. This phenomena can be observed in all $Zn_{1-x}Co_xO$ NWs having different diameters and Co-concentrations. It implies that a high-vacuum annealing produces oxygen vacancies (zinc interstitials) to enhance a ferromagnetic interaction between Co ions and to intensify a magnetic state.

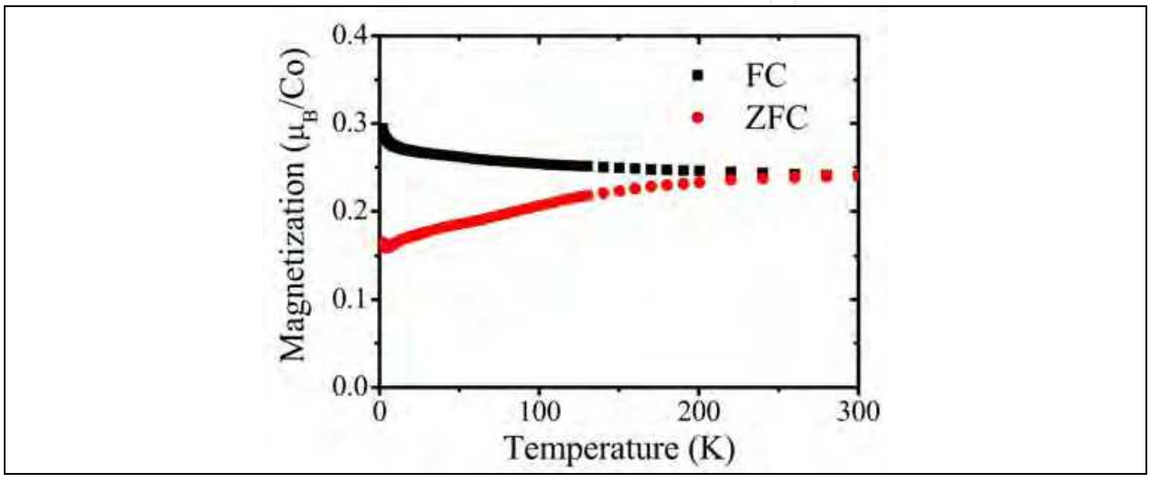

Fig. 10. FC and ZFC magnetization of ZnO sheathed in amorphous carbon with Co clusters. The Co ion dose and average diameter of ZnO are 4×10^{16} cm^{-2} and 38 nm, respectively, for this sample.

The temperature dependent behavior of ZnO sheathed in amorphous carbon with Co clusters is presented in Fig. 10. FC and ZFC magnetizations are separated into two parts with a decrease of temperature. The undeniable bifurcation of temperature dependent magnetization in FC and ZFC procedures stands for a superparamagnetic feature of ferromagnetic collloids of Co clusters (Bean & Livingston, 1959). This feature will be evident if the Co clusters are monodispersed and uniform in size. As we have shown in Fig. 6(f), the Co clusters have a wide distribution and a standard deviation of ~6.0 nm in diameter that causes a relatively small deviation in FC and ZFC magnetization at low temperatures in comparison with ideal ferromagnetic colloids. The magnitude of several tenths of μ_B in magnetization is in the same order of magnitude as that of DMS $Zn_{1-x}Co_xO$ NWs (see Fig. 9). This finding indicates that magnetic moments of cluster samples and DMS $Zn_{1-x}Co_xO$ NWs do originate from aggregated Co nanoparticles and non-aggregated Co ions, respectively.

5.2 Field dependent magnetization

In addition to a temperature dependent behavior, data of field dependent magnetizations as well as hysteresis loops were taken at several different temperatures. Figure 11 exhibits hysteresis loops of as-implanted $Zn_{1-x}Co_xO$ NWs. Having an equal Co-concentration of 8%,

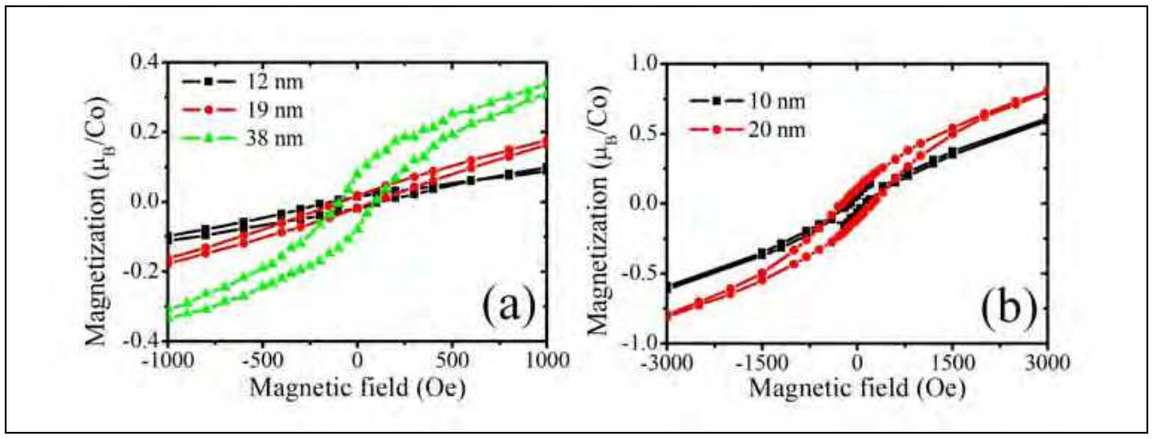

Fig. 11. (a) Hysteresis loops of as-implanted $Zn_{0.92}Co_{0.08}O$ NWs with three different average diameters marked on graph. The data were taken at 5 K. (b) Hysteresis loops of as-implanted $Zn_{0.96}Co_{0.04}O$ NWs with two different average diameters marked on graph. The data were taken at 2 K.

thick NWs reveal a high magnetization and a larger hysteresis loop (see Fig. 11(a)). Figure 11(b) presents a similar manner of a size dependence to convince us this general phenomena observed in as-implanted $Zn_{1-x}Co_xO$ NWs. The consequence of a high magnetization in thick NWs agrees with the temperature dependence delineated in Fig. 9(a).

We have argued that the implantation of a high beam current of 600 nA/cm^2 could somewhat introduce a high-vacuum annealing and create oxygen vacancies (zinc interstitials) in ZnO NWs so as to turn on an exchange interaction between non-aggregated Co ions. The Co ions occupying in a certain volume of a ZnO form a magnetic domain. If the ZnO is cut into smaller pieces such as NWs, the magnetic domain and magnetization (moment) will be abated and reduced. This splitting and diminishing of magnetic domains lead to the size effect observed in as-implanted $Zn_{1-x}Co_xO$ NWs. Moreover, the small hysteresis loop indicating a low coercive field (force) in thin $Zn_{1-x}Co_xO$ NWs may be due to a weak interaction between size-reduced magnetic domains or to planar defects (stacking faults and streaking) induced a reduction of ferromagnetic interactions.

We have observed an increase in magnetization from temperature dependent studies after a high-vacuum annealing (Section 5.1). To learn the annealing effect, multiple steps of high-vacuum annealing for hours are employed and the field dependent magnetizations are investigated after each step of annealing. Figure 12(a) and (b) demonstrate a change in hysteresis loops of $Zn_{0.92}Co_{0.08}O$ NWs with average diameters of 38 and 19 nm after each step of a high-vacuum annealing. The magnetization as well as the loop becomes higher and larger after several steps of high-vacuum annealing. The results of multiple-step annealing implies a diffusion of composing elements of the $Zn_{1-x}Co_xO$ material. It has been confirmed from EDX, EELS mapping, and high-resolution TEM inspections that the annealing will not induce detectable diffusion and clustering of Co ions in the DMS NWs. We argued, therefore, that the annealing effect produces oxygen vacancies (zinc interstitials) to enhance an exchange interaction between Co ions.

In addition to the dependence of annealing time, different surface ratios of thin and thick NWs may give rise to dissimilar responses to annealing time. Figure 12(b) reveals a larger increase and expansion in magnetization and field-dependent loops for thinner (19-nm average diameter) NWs. A decrease of annealing time and steps for thinner $Zn_{1-x}Co_xO$ NWs is due to a

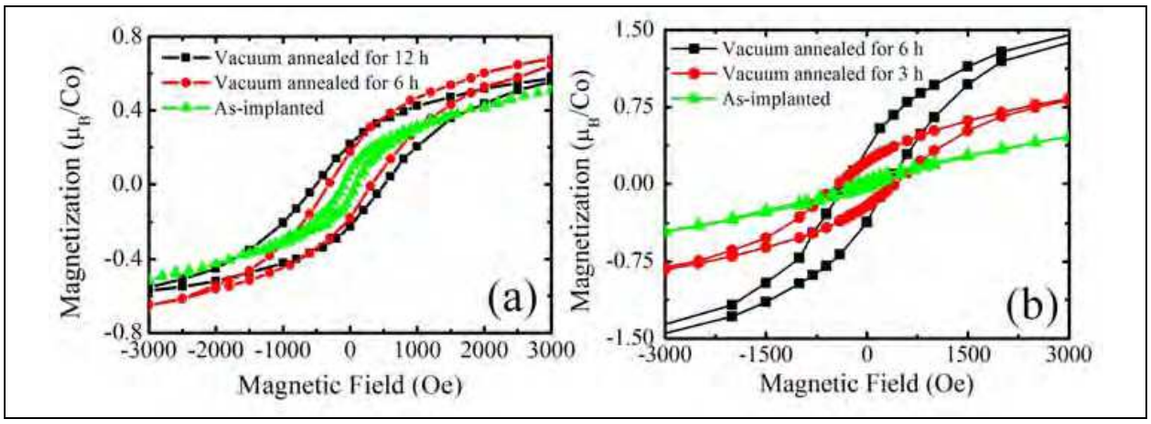

Fig. 12. (a) Hysteresis loops, taken at 10 K, of as-implanted, 6-h vacuum annealed, and 12-h vacuum annealed $Zn_{0.92}Co_{0.08}O$ NWs with a 38-nm average diameter. (b) Hysteresis loops, taken at 2 K, of as-implanted, 3-h vacuum annealed, and 6-h vacuum annealed $Zn_{0.92}Co_{0.08}O$ NWs with a 19-nm average diameter.

large surface-to-volume ratio for oxygen diffusion and a large increase in magnetization could be related to the above-mentioned reduction of magnetization in thinner NWs. To confirm the creation of oxygen vacancies during the high-vacuum annealing process, the sample is annealed in oxygen to exhibit a weak magnetic state of a low magnetization and small a hysteresis loop (not shown here), and they are subsequently annealed in a high vacuum to recover a strong magnetic state in high-vacuum annealed $Zn_{1-x}Co_xO$ NWs.

To learn more about the high-vacuum annealing enhancement of ferromagnetic ordering, temperature dependence of hysteresis loops of $Zn_{0.92}Co_{0.08}O$ NWs with 70-nm average diameter are displayed in Fig. 13(a). Unlike a bulk magnet which shows a weak temperature dependence of hysteresis loops, the DMS NWs display a strong temperature dependence as presented in Fig. 13(a). They exhibit the largest hysteresis loop at 2 K and a shrinkage of the loop like a paramagnetic linear response above room temperature. We infer that a splitting and dividing of magnetic domains (from bulk) into a small volume in NWs leads to a strong temperature dependence of hysteresis loops. This phenomena is similar to a

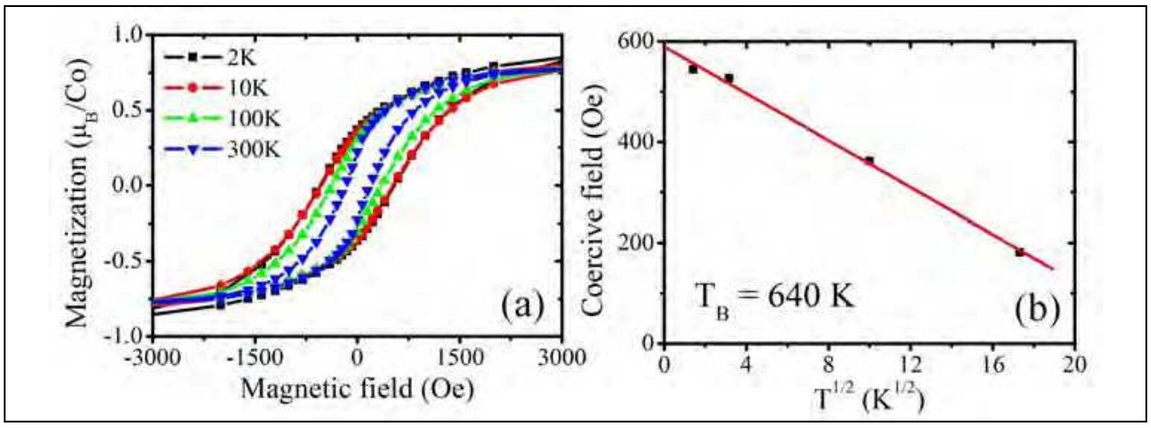

Fig. 13. (a) Hysteresis loops of $Zn_{0.92}Co_{0.08}O$ NWs with 70-nm average diameter at several temperatures after annealing in a high vacuum for 12 h. (b) The coercive field, estimated from Fig. 13(a), as a function of square root of temperature.

superparamagnetic effect on ferromagnetic colloids or magnetic clusters. On the other hand, if the exchange interaction is mediated by oxygen vacancies (zinc interstitials), a random distribution of these vacancies in $Zn_{1-x}Co_xO$ NWs could give a oxygen-vacancy depleted and non-ferromagnetic regime. This non-ferromagnetic regime separates and splits magnetic domains of non-aggregated Co ions into smaller ones. An analysis method similar to that used in a study of superparamagnetism is employed and the coercive fields evaluated from Fig. 13(a) are presented as a function of square root of temperature in Fig. 13(b). A linear dependence can be derived appreciably.

On the contrary, if we assume that the temperature dependent coercivity is originated from Co clusters, we may estimate the cluster diameter according to the equation (McHenry et al., 1994):

$$T_B = \frac{K\langle V \rangle}{30k_B}, \tag{1}$$

where T_B is the blocking temperature, $K \approx 5 \times 10^6$ erg/cm^3 is the anisotropy energy of Co metal, k_B is the Boltzmann constant, and $\langle V \rangle$ is the average volume of Co clusters. The T_B can be estimated to be 640 K from the x-axis intercept of the red fitting line in Fig. 13(b). Assume a spherical geometry for Co clusters, an average diameter of ~9 nm is derived. Such a large cluster of ~9 nm in diameter, if any exist, should be detectable in electron microscopy analyses. The Co clusters are nevertheless invisible in electron microscopy images. The temperature dependence of coercivity is therefore owing to magnetic domains formed by non-aggregated Co ions in ZnO NWs. Moreover, Fig. 13(a) demonstrates a temperature independence of magnetization saturation that is consistent with the result shown in Fig. 9(b). The ferromagnetic ordering remains up to room temperature so the RTFM in the high-vacuum annealed $Zn_{1-x}Co_xO$ NWs is confirmed.

The field dependent magnetization of the Co clustering sample at various temperatures is displayed in Fig. 14 for a comparative study. The superparamagnetic attribute of a shrinkage of hysteresis loops as well as a decrease in coercive fields with increasing temperature is perceived. The non-vanishing magnetization and coercive field at 300 K implicate that both the Curie and blocking temperatures, T_C and T_B, are above room temperature. The coercive field as a function of square root of temperature is delineated in the inset of Fig. 14. The data are fitted according to the equation (McHenry et al., 1994):

$$H_C(T) = H_C(0)\left(1 - \sqrt{T / T_B}\right), \tag{2}$$

where $H_C(T)$ and $H_C(0)$ are coercive fields at temperatures T and 0 K, respectively. The blocking temperature is determined to be ~420 K via a least square fitting, shown as a red line in the inset of Fig. 14. The average diameter of ~9 nm can be estimated by using Eq. 1 with T_B = 420 K. The average diameter of ~9 nm agrees very well with that calculated from a statistical distribution of cluster diameters from TEM measurements (9.4 nm in Fig. 6(f)). This result sustains the analyses and deductions used in this work. It is noted that all of the three characteristics of superparamagnetic Co clusters as well as ferromagnetic colloids have been observed. These features are a bifurcation of FC and ZFC magnetication (Fig. 10), a temperature dependent coercive field (Fig. 14), and the same average diameter evaluated from both TEM measurements (Fig. 6(f)) and T_B estimations (Eq. 2). It is emphasized that a wide distribution in cluster diameters (standard deviation of ~6.0 nm in this case) could smooth out superparamagnetic characteristics.

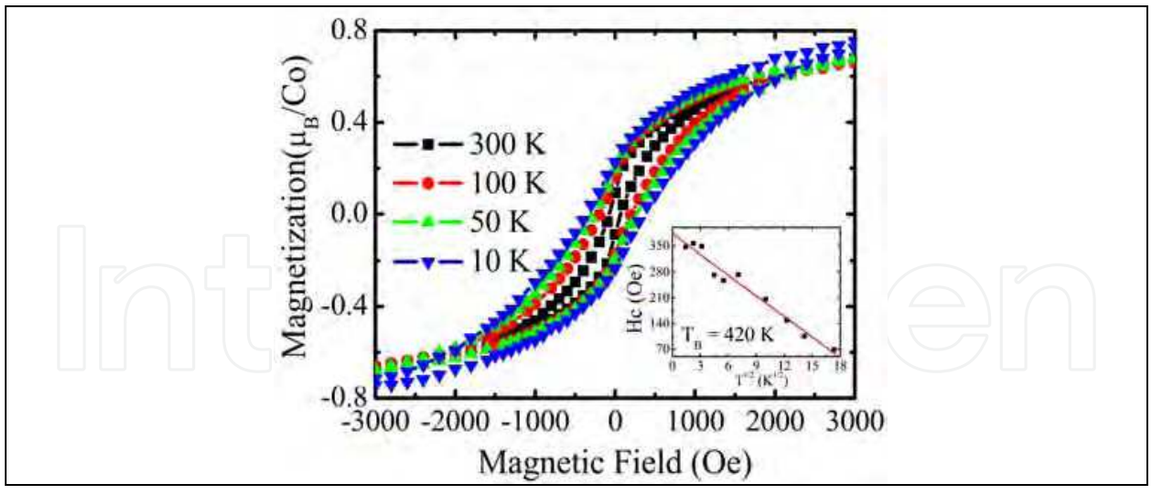

Fig. 14. Hysteresis loops of ZnO sheathed in amorphous carbon with Co clusters. The Co ion dose and average diameter of ZnO are 4×10^{16} cm^{-2} and 38 nm, respectively. The inset shows the coercive field as a function of square root of temperature.

In contrast to Co clustering samples, as-implanted (DMS) $Zn_{1-x}Co_xO$ NWs display a slight distinction between FC and ZFC magnetization in Fig. 9. After a high-vacuum annealing, FC and ZFC magnetization of DMs NWs cannot be separated from each other. High-vacuum annealed $Zn_{1-x}Co_xO$ NWs present a temperature dependence of hysteresis loops and coercive fields as shown in Fig. 13. Such a large cluster diameter of ~9 nm is estimated from the temperature dependent coercivity, but no perceptible Co clusters have ever been detected in $Zn_{1-x}Co_xO$ NWs (see Fig. 6). The Co ions in the NWs show non-aggregated random distribution (see Fig. 7) before and even after annealing in a high vacuum. It is conjectured, therefore, that a magnetic domain could be composed of non-aggregated Co ions in $Zn_{1-x}Co_xO$ NWs. Field dependent magnetization shown in Fig. 12 endorses our conjecture. Further, a vacuum annealing can help to generate oxygen vacancies (zinc interstitials) and induce a ferromagnetic interaction between Co ions. Moreover, the size effect shown in Figs. 9 and 11 implicates that $Zn_{1-x}Co_xO$ NWs, like a large magnetic domain in bulk being cut into small pieces, may reveal a relatively low magnetization as well as a weak magnetic state. That is why the $Zn_{1-x}Co_xO$ NWs exhibit superparamagnetic features. Through a systematic analysis and a comparative study with Co clustering samples, we come to a conclusion that $Zn_{1-x}Co_xO$ NWs are a DMS material. Moreover, a ferromagnetic order in $Zn_{1-x}Co_xO$ NWs remains up to room temperature, implying the RTFM in this particular material.

6. Conclusion

Various average diameters of single-crystalline, either cylindrical or hexagonal ZnO NWs with a [0001] growth direction are synthesized by using the vapor transport method. The diameters of cylindrical ZnO NWs can be well regulated by using gold nanoparticles as catalysts while the diameters of hexagonal NWs have a wide statistical distribution. The hexagonal NWs show straight in the growth direction whereas the cylindrical NWs show a bending feature, structure defects of stacking faults and point defects, and bumpy surfaces. The thinner the NWs are the higher the structure defect density and the more obvious the bending manner exist. In addition, the optical properties of thin ZnO NWs show a stronger green defect emission.

The as-grown ZnO NWs are implanted with different doses of Co ions to form $Zn_{1-x}Co_xO$ NWs ($x < 0.12$). The as-implanted $Zn_{1-x}Co_xO$ NWs possess a high density of bombardment-induced structure defects and exhibit either a paramagnetic or a weak ferromagnetic state. Thinner as-implanted $Zn_{1-x}Co_xO$ NWs exhibit a larger hysteresis loop and a higher magnetization. This NW-diameter dependence indicates that a bulk magnet with a large magnetic domain is divided into many pieces of NWs with lots of small-size domains. Annealing in a high vacuum reduces structural, planar defects of stacking faults and streaking, and creates point defects of oxygen vacancies (zinc interstitials) in $Zn_{1-x}Co_xO$ NWs to induce a strong ferromagnetic state. By using EDX mapping, it is observed that Co ions are randomly distributed without any aggregations in both as-implanted and annealed $Zn_{1-x}Co_xO$ NWs. The annealing effect further supports the idea of oxygen vacancies (zinc interstitials) induced ferromagnetic interactions between Co ions. Moreover, an oxygen-vacancy depleted, non-magnetic regime and a NW-divided small volume give rise to a separation and partition of a ferromagnetic domain, leading to a superparamagnetic feature. After high-vacuum annealing, more oxygen vacancies are generated and the magnetic domains grow up. The superparamagnetic features gradually disappear in the high-vacuum annealed $Zn_{1-x}Co_xO$ NWs. The ferromagnetic properties are observed at room temperature to assure the RTFM in the high-vacuum annealed $Zn_{1-x}Co_xO$ NWs, and to confirm the T_C above room temperature.
In particular, ZnO NWs sheathed in amorphous carbon with Co clusters have been produced after annealing in a high vacuum. The clustering sample show superparamagnetic features of FC and ZFC magnetization separation, temperature dependent coercivities, and a blocking temperature with which average diameters of Co clusters have been evaluated. The result of a comparative study with Co clustering samples corroborates our measurements and analyses of DMS $Zn_{1-x}Co_xO$ NWs.

7. Acknowledgments

This work was supported by the Taiwan National Science Council under Grant No. NSC 95-2112-M-009-045-MY3 and by the MOE ATU Program. The magnetization measurements were performed on a SQUID magnetometer (MPMS XL-7) at the National Chiao Tung University.

8. References

Baibich, M. N.; Broto, J. M.; Fert, A.; Nguyen Van Dau, F.; Petroff, F.; Eitenne, P.; Creuzet, G.; Friederich, A. & Chazelas, J. (1988). Giant Magnetoresistance of (001)Fe/(001)Cr Magnetic Superlattices. *Phys. Rev. Lett.*, Vol. 61, pp. 2472-2475.

Bean, C. P. & Livingston, J. D. (1959). Superparamagnetism. *J. Appl. Phys.*, Vol. 30, pp. 120S-129S.

Behan, A. J.; Mokhtari, A.; Blythe, H. J.; Score, D.; Xu, X. H.; Neal, J. R.; Fox, A. M. & Gehring, G. A. (2008). Two Magnetic Regimes in Doped ZnO Corresponding to a Diluted Magnetic Semiconductor and a Diluted Magnetic Insulator. *Phys. Rev. Lett.*, Vol. 100, p. 047206.

Binasch, G.; Grünberg, P.; Saurenbach F. & Zinn, W. (1989). Enhanced magnetoresistance in layered magnetic structures with antiferromagnetic interlayer exchange. *Phys. Rev. B*, Vol. 39, pp. 4828-4830.

Chen, I. J.; Ou, Y. C.; Wu, Z. Y.; Chen, F. R.; Kai, J. J.; Lin, J. J. & Jian, W. B. (2008). Size Effects on Thermal Treatments and Room-Temperature Ferromagnetism in High-Vacuum Annealed ZnCoO Nanowires. *J. Phys. Chem. C*, Vol. 112, pp. 9168-9171.

Chiba, D.; Yamanouchi, M.; Matsukura, F. & Ohno, H. (2003). Electrical Manipulation of Magnetization Reversal in a Ferromagnetic Semiconductor. *Science*, Vol. 301, pp. 943-945.

Cho, S.; Choi, S.; Cha, G. B.; Hong, S. C.; Kim, Y.; Zhao, Y. J.; Freeman, A. J.; Ketterson, J. B.; Kim, B. J.; Kim, Y. C.; Choi, B. C. (2002). Room-Temperature Ferromagnetism in $(Zn_{1-x}Mn_x)GeP_2$ Semiconductors. *Phys. Rev. Lett.*, Vol. 88, p. 257203.

Coey, J. M. D.; Venkatesan, M. & Fitzgerald, C. B. (2005). Donor impurity band exchange in dilute ferromagnetic oxides. *Nat. Mater.*, Vol. 4, pp. 173-179.

Dieny, B.; Speriosu, V. S.; Parkin, S. S. P.; Gurney, B. A.; Wilhoit, D. R. & Mauri, D. (1991). Giant Magnetoresistance in soft ferromagnetic multilayers. *Phys. Rev. B*, Vol. 43, pp. 1297-1300.

Dietl, T.; Ohno, H.; Matsukura, F.; Cibert, J. & Ferrand, D. (2000). Zener Model Description of Ferromagnetism in Zinc-Blende Magnetic Semiconductors. *Science*, Vol. 287, pp. 1019-1022.

Furdyna, J. K. (1988). Diluted magnetic semiconductors. *J. Appl. Phys.*, Vol. 64, pp. R29-R64.

Hayashi, T.; Shimada, H.; Shimizu, H. & Tanaka, M. (1999). Tunneling spectroscopy and tunneling magnetoresistance in (GaMn)As ultrathin heterostructures. *J. Cryst. Growth*, Vol. 201/202, pp. 689-692.

Janisch, R.; Gopal, P. & Spaldin, N. A. (2005). Transition metal-doped TiO2 and ZnO--present status of the field. *J. Phys. Condens. Mater.*, Vol. 17, pp. R657-R689.

Jian, W. B.; Wu, Z. Y.; Huang, R. T.; Chen, F. R.; Kai, J. J.; Wu, C. Y.; Chiang, S. J.; Lan, M. D. & Lin, J. J. (2006). Direct observation of structure effect on ferromagnetism in $Zn_{1-x}Co_xO$ nanowires. *Phys. Rev. B*, Vol. 73, p. 233308.

Jian, W. B.; Chen, I. J.; Liao, T. C.; Ou, Y. C.; Nien, C. H.; Wu, Z. Y.; Chen, F. R.; Kai, J. J. & Lin, J. J. (2007). Size Dependent Magnetization and High-Vacuum Annealing Enhanced Ferromagnetism in $Zn_{1-x}Co_xO$ Nanowires. *J. Nanosci. Nanotechnol.*, Vol. 8, pp. 202-211.

Klingshirn, C. (2007). ZnO : Material, Physics and Applications. *ChemPhysChem*, Vol. 8, pp. 782-803.

Lany, S. & Zunger, A. (2005). Anion vacancies as a source of persistent photoconductivity in II-VI and chalcopyrite semiconductors. *Phys. Rev. B*, Vol. 72, p. 035215.

Lany, S. & Zunger, A. (2007). Dopability, Intrinsic Conductivity, and Nonstoichiometry of Transparent Conducting Oxides. *Phys. Rev. Lett.*, Vol. 98, p. 045501.

Look, D. C.; Hemsky, J. W. & Sizelove, J. R. (1999). Residual Native Shallow Donor in ZnO. *Phys. Rev. Lett.*, Vol. 82, pp. 2552-2555.

Look, D. C.; Farlow, G. C.; Reunchan, P.; Limpijumnong, S.; Zhang, S. B. & Nordlund, K. (2005). Evidence for Native-Defect Donors in *n*-Type ZnO. *Phys. Rev. Lett.*, Vol. 95, p. 225502.

McHenry, M. E.; Majetich, S. A.; Artman, J. O.; DeGraef, M. & Staley, S. W. (1994). Superparamagnetism in carbon-coated Co particles produced by the Kratschmer carbon arc process. *Phys. Rev. B*, Vol. 49, pp. 11358-11363.

Matsumoto, Y.; Murakami, M.; Shono, T.; Hasegawa, T.; Fukumura, T.; Kawasaki, M.; Ahmet, P.; Chikyow, T.; Koshihara, S. & Koinuma, H. (2001). Room-Temperature Ferromagnetism in Transparent Transition Metal-Doped Titanium Dioxide. *Science*, Vol. 291, pp. 854-856.

Moodera, J. S.; Kinder, L. R.; Wong, T. M. & Meservey, R. (1995). Large Magnetoresistance at Room Temperature in Ferromagnetic Thin Film Tunnel Junctions. *Phys. Rev. Lett.*, Vol. 74, pp. 3273-3276.

Neal, J. R.; Behan, A. J.; Ibrahim, R. M.; Blythe, H. J.; Ziese, M.; Fox, A. M. & Gehring, G. A. (2006). Room-Temperature Magneto-Optics of Ferromagnetic Transition-Metal-Doped ZnO Thin Films. *Phys. Rev. Lett.*, Vol. 96, p. 197208.

Ohno, H.; Shen, A.; Matsukura, F.; Oiwa, A.; Endo, A.; Katsumoto, S. & Iye, Y. (1996). (Ga,Mn)As : A new diluted magnetic semiconductor based on GaAs. *Appl. Phys. Lett.*, Vol. 69, pp. 363-365.

Ohno, H. (1998). Making Nonmagnetic Semiconductors Ferromagnetic. *Science*, Vol. 281, pp. 951-956.

Ohno, H.; Chiba, D.; Matsukura, F.; Omiya, T.; Abe, E.; Dietl, T., Ohno, Y. & Ohtani, K. (2000). Electric-field control of ferromagnetism. *Nature*, Vol. 408, pp. 944-946.

Ohno, Y.; Young, D. K.; Beschoten, B.; Matsukura, F.; Ohno, H. & Awschalom, D. D. (1999). Electrical spin injection in a ferromagnetic semiconductor heterostructure. *Nature*, Vol. 402, pp. 790-792.

Pearton, S. J.; Norton, D. P.; Ip, K.; Heo, Y. W. & Steiner, T. (2004). Recent advances in processing of ZnO. *J. Vac. Sci. Technol. B*, Vol. 22, pp. 932-948.

Prinz, G. A. (1998). Magnetoelectronics. *Science*, Vol. 282, pp. 1660-1663.

Risbud, A. S.; Spaldin, N. A.; Chen, Z. Q.; Stemmer, S. & Seshadri, R. (2003). Magnetism in polycrystalline cobalt-substituted zinc oxide. *Phys. Rev. B*, Vol. 68, p. 205202.

Sati, P.; Deparis, C.; Morhain, C.; Schäfer, S. & Stepanov, A. (2007). Antiferromagnetic Interactions in Single Crystalline $Zn_{1-x}Co_xO$ Thin Films. *Phys. Rev. Lett.*, Vol. 98, p. 137204.

Schwartz, D. A. & Gamelin, D. R. (2004). Reversible 300 K Ferromagnetic Ordering in a Diluted Magnetic Semiconductor. Adv. Mater., Vol. 16, pp. 2115-2119.

Story, T.; Galazka, R. R.; Frankel, R. B. & Wolff, P. A. (1986). Carrier-Concentration-Induced Ferromagnetism in PbSnMnTe. *Phys. Rev. Lett.*, Vol. 56, pp. 777-779.

Sawicki, M.; Dietl, T.; Kossut, J.; Igalson, J.; Wojtowicz, T. & Plesiewicz, W. (1986). Influence of s-d Exchange Interaction on the Conductivity of $Cd_{1-x}Mn_xSe$:In in the Weakly Localized Regime. *Phys. Rev. Lett.*, Vol. 56, pp. 508-511.

Toyosaki, T.; Fukumura, T.; Yamada, Y.; Nakajima, K.; Chikyow, T.; Hasegawa, T.; Koinuma, H. & Kawasaki, M. (2004). Anomalous Hall effect governed by electron doping in a room-temperature transparent ferromagnetic semiconductor. *Nat. Mater.*, Vol. 3, pp. 221-224.

Ueda, K.; Tabata, H. & Kawaib, T. (2001). Magnetic and electric properties of transition-metal-doped ZnO films. *Appl. Phys. Lett.*, Vol. 79, pp. 988-990.

Van de Walle, C. G. (2000). Hydrogen as a Cause of Doping in Zinc Oxide. *Phys. Rev. Lett.*, Vol. 85, pp. 1012-1015.

Wolf, S. A.; Awschalom, D. D.; Buhrman, R. A.; Daughton, J. M.; S. von Molnár, Roukes, M. L.; Chtchelkanova, A. Y. & Treger, D. M. (2001). Spintronics: A Spin-Based Electronics Vision for the Future. *Science*, Vol. 294, pp. 1488-1495.

Wu, Z. Y.; Chen, F. R.; Kai, J. J.; Jian W. B. & Lin, J. J. (2006). Fabrication, characterization and studies of annealing effects on ferromagnetism in $Zn_{1-x}Co_xO$ nanowires. *Nanotechnology*, Vol. 17, pp. 5511-5518.

Wu, Z. Y.; Chen, I. J.; Lin, Y. F.; Chiu, S. P.; Chen, F. R.; Kai, J. J.; Lin, J. J. & Jian W. B. (2008). Cross-sectional shape modulation of physical properties in ZnO and $Zn_{1-x}Co_xO$ nanowies. *New J. Phys.*, Vol. 10, p. 033017.

Xu, Q.; Hartmann, L.; Zhou, S.; Mcklich, A.; Helm, M.; Biehne, G.; Hochmuth, H.; Lorenz, M.; Grundmann, M. & Schmidt, H. (2008). Spin Manipulation in Co-doped ZnO. *Phys. Rev. Lett.*, Vol. 101, p. 076601.

Yamanouchi, M.; Chiba, D.; Matsukura, F. & Ohno, H. (2004). Current-induced domain-wall switching in a ferromagnetic semiconductor structure. *Nature*, Vol. 428, pp. 539-542.

Zhang, Z. H.; Wang, X.; Xu, J. B.; Muller, S.; Ronning, C. & Li, Q. (2009). Evidence of intrinsic ferromagnetism in individual dilute magnetic semiconducting nanostructures. *Nat. Nanotechnol.*, Vol. 4, pp. 523-527.

Nanowires

Edited by Paola Prete

ISBN 978-953-7619-79-4
Hard cover, 414 pages
Publisher InTech
Published online 01, February, 2010
Published in print edition February, 2010

This volume is intended to orient the reader in the fast developing field of semiconductor nanowires, by providing a series of self-contained monographs focusing on various nanowire-related topics. Each monograph serves as a short review of previous results in the literature and description of methods used in the field, as well as a summary of the authors recent achievements on the subject. Each report provides a brief sketch of the historical background behind, the physical and/or chemical principles underlying a specific nanowire fabrication/characterization technique, or the experimental/theoretical methods used to study a given nanowire property or device. Despite the diverse topics covered, the volume does appear as a unit. The writing is generally clear and precise, and the numerous illustrations provide an easier understanding of the phenomena described. The volume contains 20 Chapters covering altogether many (although not all) semiconductors of technological interest, starting with the IV-IV group compounds (SiC and SiGe), carrying on with the binary and ternary compounds of the III-V (GaAs, AlGaAs, GaSb, InAs, GaP, InP, and GaN) and II-VI (HgTe, HgCdTe) families, the metal oxides (CuO, ZnO, ZnCoO, tungsten oxide, and PbTiO3), and finishing with Bi (a semimetal).

How to reference

In order to correctly reference this scholarly work, feel free to copy and paste the following:

Yi-Ching Ou, Zhong-Yi Wu, Fu-Rong Chen, Ji-Jung Kai and Wen-Bin Jian (2010). Characterization of Room-Temperature Ferromagnetic Zn1-xCoxO Nanowires, Nanowires, Paola Prete (Ed.), ISBN: 978-953-7619-79-4, InTech, Available from: http://www.intechopen.com/books/nanowires/characterization-of-room-temperature-ferromagnetic-zn1-xcoxo-nanowires

INTECH
open science | open minds

InTech Europe
University Campus STeP Ri
Slavka Krautzeka 83/A
51000 Rijeka, Croatia
Phone: +385 (51) 770 447
Fax: +385 (51) 686 166
www.intechopen.com

InTech China
Unit 405, Office Block, Hotel Equatorial Shanghai
No.65, Yan An Road (West), Shanghai, 200040, China
中国上海市延安西路65号上海国际贵都大饭店办公楼405单元
Phone: +86-21-62489820
Fax: +86-21-62489821

IntechOpen